Picosecond-pulsed laser ablation of zinc: crater morphology and comparison of methods to determine ablation threshold

H. MUSTAFA,[1,*] R. POHL,[1] T. C. BOR,[2] B. PATHIRAJ,[1] D. T. A. MATTHEWS,[1,3,4] AND G. R. B. E. RÖMER[1]

[1] *Chair of Laser Processing, Department of Mechanics of Solids, Surfaces & Systems (MS³), Faculty of Engineering Technology, University of Twente, Enschede, the Netherlands*
[2] *Chair of Production Technology, Department of Mechanics of Solids, Surfaces & Systems (MS³), Faculty of Engineering Technology, University of Twente, Enschede, the Netherlands*
[3] *Chair of Skin Tribology, Department of Mechanics of Solids, Surfaces & Systems (MS³), Faculty of Engineering Technology, University of Twente, Enschede, the Netherlands*
[4] *Tata Steel Research and Development, IJmuiden, the Netherlands*
[*] *h.mustafa@utwente.nl*

Abstract: Ablation of bulk polycrystalline zinc in air is performed with single and multiple picosecond laser pulses at a wavelength of 1030 nm. The relationships between the characteristics of the ablated craters and the processing parameters are analyzed. Morphological changes of the ablated craters are characterized by means of scanning electron microscopy and confocal laser scanning microscopy. Chemical compositions of both the treated and untreated surfaces are quantified with X-ray photoelectron spectroscopy. A comparative analysis on the determination of the ablation threshold using three methods, based on ablated diameter, depth and volume is presented along with associated incubation coefficients. The single pulse ablation threshold value is found to equal 0.21 J/cm². Using the calculated incubation coefficients, it is found that both the fluence threshold and energy penetration depth show lesser degree of incubation for multiple laser pulses.

OCIS codes: (140.3390) Laser materials processing; (140.7090) Ultrafast lasers; (140.3330) Laser damage.

References and links

1. D. Zhang and L. Guan, "Laser Ablation" in *Comprehensive Materials Processing*, S. Hashmi, G. F. Batalha, C. J. van Tyne, B. S. Yilbas, ed. (Elsevier, 2014).
2. H. Costa and I. Hutchings, "Some innovative surface texturing techniques for tribological purposes," Proc. Inst. Mech. Eng. Part J: J. Eng. Tribol. **229**, 429–448 (2015).
3. R. Fang, A. Vorobyev, and C. Guo, "Direct visualization of the complete evolution of femtosecond laser-induced surface structural dynamics of metals," Light. Sci. Appl. **6** (2017).
4. A. Klini, P. Loukakos, D. Gray, A. Manousaki, and C. Fotakis, "Laser induced forward transfer of metals by temporally shaped femtosecond laser pulses," Opt. express **16**, 11300–11309 (2008).
5. J. Liu, "Simple technique for measurements of pulsed Gaussian-beam spot sizes," Opt. letters **7**, 196–198 (1982).
6. S. Preuss, A. Demchuk, and M. Stuke, "Sub-picosecond UV laser ablation of metals," Appl. Phys. A: Mater. Sci. & Process. **61**, 33–37 (1995).
7. G. Račiukaitis, M. Brikas, P. Gecys, and M. Gedvilas, "Accumulation effects in laser ablation of metals with high-repetition-rate lasers," in High-Power Laser Ablation 2008, (International Society for Optics and Photonics, 2008), pp. 70052L–70052L.
8. L. Cabalin and J. Laserna, "Experimental determination of laser induced breakdown thresholds of metals under nanosecond Q-switched laser operation," Spectrochimica Acta Part B: At. Spectrosc. **53**, 723–730 (1998).
9. A. R. Kumar, G. Padmaja, P. Radhakrishnan, V. Nampoori, and C. Vallabhan, "Evaluation of laser ablation threshold in polymer samples using pulsed photoacoustic technique," Pramana. **37**, 345–351 (1991).
10. N. Hosoya, I. Kajiwara, T. Inoue, and K. Umenai, "Non-contact acoustic tests based on nanosecond laser ablation: generation of a pulse sound source with a small amplitude," J. Sound Vib. **333**, 4254–4264 (2014).
11. E. G. Gamaly, N. Madsen, M. Duering, A. V. Rode, V. Z. Kolev, and B. Luther-Davies, "Ablation of metals with picosecond laser pulses: evidence of long-lived nonequilibrium conditions at the surface," Phys. Rev. B **71**, 174405 (2005).

12. K. H. Leitz, B. Redlingshöfer, Y. Reg, A. Otto, and M. Schmidt, "Metal ablation with short and ultrashort laser pulses," Phys. Procedia **12**, 230–238 (2011).

13. B. Neuenschwander, B. Jaeggi, M. Schmid, and G. Hennig, "Surface structuring with ultra-short laser pulses: basics, limitations and needs for high throughput," Phys. Procedia **56**, 1047–1058 (2014).

14. J. Byskov-Nielsen, J. M. Savolainen, M. S. Christensen, and P. Balling, "Ultra-short pulse laser ablation of metals: threshold fluence, incubation coefficient and ablation rates," Appl. Phys. A: Mater. Sci. & Process. **101**, 97–101 (2010).

15. Y. Jee, M. F. Becker, and R. M. Walser, "Laser-induced damage on single-crystal metal surfaces," J. Opt. Soc. Am. B **5**, 648–659 (1988).

16. M. Hashida, A. F. Semerok, O. Gobert, G. Petite, and J. F. Wagner, "Ablation thresholds of metals with femtosecond laser pulses," in Nonresonant Laser-Matter Interaction (NLMI-10), (International Society for Optics and Photonics, 2001), pp. 178–185.

17. P. Mannion, J. Magee, E. Coyne, G. O'Connor, and T. Glynn, "The effect of damage accumulation behaviour on ablation thresholds and damage morphology in ultrafast laser micro-machining of common metals in air," Appl. Surf. Sci. **233**, 275–287 (2004).

18. B. Neuenschwander, G. Bucher, G. Hennig, C. Nussbaum, B. Joss, M. Muralt, S. Zehnder, U. W. Hunziker, and P. Schuetz, "Processing of dielectric materials and metals with ps laser pulses," in Proceedings of the 29th International Congress on Applications of Lasers & Electro-Optics (ICALEO), Anaheim, California, (2010).

19. B. Neuenschwander, B. Jaeggi, M. Schmid, V. Rouffiange, and P. E. Martin, "Optimization of the volume ablation rate for metals at different laser pulse-durations from ps to fs," in SPIE LASE, (International Society for Optics and Photonics, 2012), pp. 824307–824307.

20. F. Di Niso, C. Gaudiuso, T. Sibillano, F. P. Mezzapesa, A. Ancona, and P. M. Lugarà, "Role of heat accumulation on the incubation effect in multi-shot laser ablation of stainless steel at high repetition rates," Opt. express **22**, 12200–12210 (2014).

21. F. C. Porter, *Zinc handbook: Properties, Processing, and Use in design* (CRC, 1991).

22. F. C. Porter, *Corrosion resistance of zinc and zinc alloys* (CRC, 1994).

23. S. S. Wellershoff, J. Hohlfeld, J. Güdde, and E. Matthias, "The role of electron–phonon coupling in femtosecond laser damage of metals," Appl. Phys. A **69**, S99–S107 (1999).

24. M. Hase, K. Ishioka, J. Demsar, K. Ushida, and M. Kitajima, "Ultrafast dynamics of coherent optical phonons and nonequilibrium electrons in transition metals," Phys. Rev. B **71**, 184301 (2005).

25. M. Butt, "Laser ablation characteristics of metallic materials: role of debye-waller thermal parameter," in IOP Conference Series: Materials Science and Engineering, , vol. 60 (Institute of Physics, 2014), pp. 012068.

26. B. Qian and Z. Shen, "Fabrication of superhydrophobic surfaces by dislocation-selective chemical etching on aluminum, copper, and zinc substrates," Langmuir **21**, 9007–9009 (2005).

27. T. H. Muster, W. D. Ganther, and I. S. Cole, "The influence of microstructure on surface phenomena: rolled zinc," Corros. Sci. **49**, 2037–2058 (2007).

28. J. Scheers, M. Vermeulen, C. De Mare, and K. Meseure, "Assessment of steel surface roughness and waviness in relation with paint appearance," Int. J. Mach. Tools Manuf. **38**, 647–656 (1998).

29. M. Agranat, S. Ashitkov, V. Fortov, A. Kirillin, A. Kostanovskii, S. Anisimov, and P. Kondratenko, "Use of optical anisotropy for study of ultrafast phase transformations at solid surfaces," Appl. Phys. A: Mater. Sci. & Process. **69**, 637–640 (1999).

30. A. Vorobyev and C. Guo, "Enhanced energy coupling in femtosecond laser-metal interactions at high intensities," Opt. express **14**, 13113–13119 (2006).

31. L. Mosteller Jr and F. Wooten, "Optical properties of Zn," Phys. Rev. **171**, 743 (1968).

32. D. Linde, *Handbook of Chemistry and Physics* (CRC, 1994).

33. M. Querry, "Optical constants of minerals and other materials from the millimeter to the ultraviolet," Tech. rep., Chemical Research Development And Engineering Center Aberdeen Proving Groundmd (1987).

34. W. Bond, "Measurement of the refractive indices of several crystals," J. Appl. Phys. **36**, 1674–1677 (1965).

35. H. J. Hagemann, W. Gudat, and C. Kunz, "Optical constants from the far infrared to the x-ray region: Mg, Al, Cu, Ag, Au, Bi, C, and Al_2O_3," J. Opt. Soc. Am. B **65**, 742–744 (1975).

36. J. Hohlfeld, S. S. Wellershoff, J. Güdde, U. Conrad, V. Jähnke, and E. Matthias, "Electron and lattice dynamics following optical excitation of metals," Chem. Phys. **251**, 237–258 (2000).

37. T. Delgado, D. Nieto, and M. T. Flores-Arias, "Soda-lime glass microlens arrays fabricated by laser: Comparison between a nanosecond and a femtosecond IR pulsed laser," Opt. Lasers Eng. **86**, 29–37 (2016).

38. J. V. Oboňa, V. Ocelík, J. Rao, J. Skolski, G. R. B. E. Römer, A. Huisin't Veld, and J. T. M. De Hosson, "Modification of Cu surface with picosecond laser pulses," Appl. Surf. Sci. **303**, 118–124 (2014).

39. J. V. Oboňa, V. Ocelík, J. Hosson, J. Skolski, V. Mitko, and G. R. B. E. Römer, "Surface melting of copper by ultrashort laser pulses," in Surface effects and contact mechanics X : computational methods and experiments, (Wessex Institute of Technology, 2011).

40. A. Miloshevsky, S. S. Harilal, G. Miloshevsky, and A. Hassanein, "Dynamics of plasma expansion and shockwave formation in femtosecond laser-ablated aluminum plumes in argon gas at atmospheric pressures," Phys. Plasmas **21**, 043111 (2014).

41. M. Tanski, M. Kocik, R. Barbucha, K. Garasz, and J. Mizeraczyk, "Time-resolved observation of the ablation

plasma plume dynamics during nanosecond laser micromachining," in Photonics and Optoelectronics (SOPO), 2012 Symposium on, (IEEE, 2012), pp. 1–4.

42. W. Falke, A. Schwaneke, and R. Nash, "Surface tension of zinc: the positive temperature coefficient," Metall. Mater. Transactions B **8**, 301–303 (1977).

43. J. Bonse, K. W. Brzezinka, and A. Meixner, "Modifying single-crystalline silicon by femtosecond laser pulses: an analysis by micro Raman spectroscopy, scanning laser microscopy and atomic force microscopy," Appl. Surf. Sci. **221**, 215–230 (2004).

44. S. Evans, "Correction for the effects of adventitious carbon overlayers in quantitative XPS analysis," Surf. Interface Analysis: An Int. J. devoted to development application techniques for analysis surfaces, interfaces thin films **25**, 924–930 (1997).

45. S. Feliu Jr and V. Barranco, "XPS study of the surface chemistry of conventional hot-dip galvanised pure Zn, galvanneal and Zn–Al alloy coatings on steel," Acta materialia **51**, 5413–5424 (2003).

46. J. Moulder, W. Stickle, P. Sobol, and K. Bomben, *Handbook of X-Ray Photoelectron Spectroscopy* (Perkin-Elmer Corporation, 1992).

47. D. R. Baer, M. H. Engelhard, A. S. Lea, P. Nachimuthu, T. C. Droubay, J. Kim, B. Lee, C. Mathews, R. Opila, L. V. Saraf, W. F. Stickle, R. M. Wallace, B. S. Wright, "Comparison of the sputter rates of oxide films relative to the sputter rate of SiO₂," J. Vac. Sci. & Technol. A: Vacuum, Surfaces, Films **28**, 1060–1072 (2010).

48. G. Račiukaitis, M. Brikas, P. Gečys, B. Voisiat, M. Gedvilas, "Use of high repetition rate and high power lasers in microfabrication: how to keep the efficiency high?" JLMN J. Laser Micro/Nanoengineering **4**, 186–191 (2009).

49. B. Neuenschwander, B. Jaeggi, M. Schmid, A. Dommann, A. Neels, T. Bandi, and G. Hennig, "Factors controlling the incubation in the application of ps laser pulses on copper and iron surfaces," Proc. SPIE 8607, 86070D (2013).

50. Z. Sun, M. Lenzner, and W. Rudolph, "Generic incubation law for laser damage and ablation thresholds," J. Appl. Phys. **117**, 073102 (2015).

51. B. Jaeggi, B. Neuenschwander, M. Schmid, M. Muralt, J. Zuercher, and U. Hunziker, "Influence of the pulse duration in the ps-regime on the ablation efficiency of metals," Phys. Procedia **12**, 164–171 (2011).

52. C. Cheng, S. Wang, K. Chang, and J. Chen, "Femtosecond laser ablation of copper at high laser fluence: modeling and experimental comparison," Appl. Surf. Sci. **361**, 41–48 (2016).

53. D. Bergström, "The absorption of laser light by rough metal surfaces," Ph.D. thesis, Luleå Tekniska Universitet, Sweden (2008).

54. N. W. Ashcroft, N. D. Mermin, and S. Rodriguez, *Solid State Physics* (American Association of Physics Teachers, 1998).

55. G. Motulevich and A. Shubin, "Optical constants of zinc," Sov. Phys. JETP **29**, 24–26 (1969).

56. R. Pohl, C. Visser, G. R. B. E. Römer, C. Sun, and D. Lohse, "Imaging of the ejection process of nanosecond laser-induced forward transfer of gold," JLMN J. Laser Micro/Nanoengineering **10**, 154 (2015).

1. Introduction

Laser surface texturing is a commonly used surface engineering process to increase surface functionality [1]. In comparison to other techniques like electric discharge texturing (EDT), chemical etching, shot blasting and electron beam texturing, laser texturing offers flexible, efficient and clean processing with more accurate control over surface features [1, 2]. Depending on the applied laser fluence, different surface structures appear in the laser irradiated zone. In this context, knowledge of the ablation threshold of a given material is fundamental towards understanding laser material interaction and the resulting surface features. In order to determine the fluence threshold in (ultra)short pulsed laser processing, several methods have been reported in literature based on, including, but not limited to,

- the lowest fluence at which surface modification is observable by means of an optical microscope [3, 4],
- geometric features of the ablated region [5–7],
- plasma emission [8],
- pulsed photoacoustic techniques [9, 10],
- ablated mass [11, 12].

Since quantitative analysis of surface texturing depends on the morphological characterization of laser ablated craters, the determination of the threshold fluence using geometric features has been widely applied [13–20].

Zinc is one of the most studied, versatile metals that finds application in e.g., galvanizing,

alloying and die casting [21]. Typically, in engineering applications, a small amount of Al is added in order to increase the castability of zinc. Due to its corrosion resistance and cathodic protection property, zinc is mainly used for prolonging the service life of steel [22]. To increase various material properties such as creep resistance, superplasticity, strength and hardness, zinc is also alloyed with copper, titanium or magnesium [21]. Although few studies exist that investigate the ablation threshold of zinc, as can be seen from Table 1, these studies address the ablation by either femtosecond or nanosecond pulse durations (τ_p), but not in the picosecond regime. Ablation threshold is known to be dependent on the characteristic electron-phonon coupling time (τ_{e-ph}) [1, 16, 23]. Pulse durations shorter than τ_{e-ph} result in a lower ablation threshold than thresholds found for longer pulse durations [16]. For incident laser fluences ranging from 0.018 to 28 J/cm^2, Hashida et al. reported multi-photon absorption, optical and thermal ablation regimes respectively for multiple laser pulse processing in fs pulse duration [16]. However, single pulse ablation threshold is not investigated in detail for pulse durations equal, or close, to $\tau_{e-ph,Zn,300K} = 7$ ps [24]. Additionally, in the works mentioned in Table 1, single crystal, high purity ($\geq$ 99.99%) optically flat ($R_a \sim 10$ nm) samples were studied. Moreover, the reported ablation threshold values in these studies show a large spread ranging from 0.022 to 1.8 J/cm^2, depending on the chosen method, see Table 1. Since zinc is a transitional hexagonal closed packed (hcp) metal with a filled d orbital and a low melting point ($T_m = 692.68$ K), comparison to other common metals, in terms of the characteristics of laser ablation, is not straightforward. For example, due to its relatively high Debye-Weller thermal parameter value B (or larger mean-squared amplitude of atomic vibration), the threshold fluence of Zn at a nanosecond pulsed laser wavelength of 1064 nm is not correlated with closed packed structure metals. This renders a higher ablation yield as well as a broader plasma plume as a function of B for Zn than for bcc and fcc metals [25]. Also, the presence of a native oxide layer on the surface of Zn is inevitable due to the extremely fast oxidation kinematics of Zn. However, the improvement in functionality of zinc by surface texturing produced either chemically or mechanically is seldom reported beyond superhydrophobicity [26], corrosion performance [27] and visual appearance [28]. Laser surface texturing can be a promising technique to achieve the above functions and broaden the use of Zn in modern applications.

Table 1. **Ablation Threshold Values of Zn Reported in Literature.**

Pulse duration	Wavelength [nm]	Fluence threshold [J/cm^2]	Method	Defined as/for	Ref.
5 ns	1064	1.42	Laser Induced Breakdown Spectroscopy	plasma threshold	[8]
	532	0.91			
	266	3.12			
~ 1 ps	780	0.5	optically detectable damage	melting threshold	[29]
70 fs	800	1.5	ablation rate	$N \leq 128$	[16]
		0.35		$N > 128$	
		0.35	D^2 method	$4 \leq F \leq 14\ J/cm^2$	
		0.2		$0.1 \leq F \leq 4\ J/cm^2$	
		0.03		$0.018 \leq F \leq 0.01\ J/cm^2$	
65 fs	800	0.052	optically detectable damage	ablation threshold	[30]
200 fs	800	0.102	optically detectable damage	Laser Induced Forward Transfer	[4]
65 fs	800	0.022	optically detectable damage	damage threshold	[3]
		0.1	Ultrafast pump-probe imaging	spallation	
		0.34		phase explosion	
		1.1-1.8		solid density plasma	

In this paper, picosecond laser surface ablation of polycrystalline zinc is presented with a focus on the thermal ablation regime. Therefore, the minimum fluence value used in this

work is about 1 J/cm^2. For fluence levels lower than 1 J/cm^2, a shift from thermal regime to a so-called optical regime and even multi-photon absorption regime is expected similar to results as observed in fs pulse duration processing for Zn e.g. by Hashida et al [16]. Moreover, majority of the literature that explores threshold fluence determination for different material determines either multiple pulse threshold value or uses maximum two methods to verify the single pulse ablation threshold along with associated incubation coefficient [13, 14, 16–20]. In contrast, incubation in polycrystalline Zn following single pulse threshold fluence is determined using three methods in this work with a twofold purpose. First, morphology as well as chemical composition prior to and after laser processing are analyzed to describe the resulting surface structures. Secondly, a comparative analysis of existing threshold fluence calculation methods is performed for multiple laser pulse irradiation at 1030 nm wavelength to find the best suited method in the picosecond regime ($\tau_p \approx \tau_{e-ph}$). Effects of damage accumulation on threshold fluence and energy penetration depth are also quantified using separate incubation coefficients.

2. Experimental setup

2.1. Laser setup

The ablation experiments were performed under atmospheric conditions using a diode pumped thin disc Yb:YAG pulsed laser source (TruMicro 5050 of Trumpf GmbH, Germany). This source emits 6.7 ps laser pulses of linearly polarized light at a central wavelength of 1030 nm and shows a nearly Gaussian power density profile ($M^2 < 1.3$). A galvo-scanner (IntelliScan14 of ScanLab GmbH, Germany), equipped with a telecentric flatfield F-theta-Ronar lens (Linos GmbH, Germany) of 80 mm focal length, was used to scan the focus of the laser beam over the surface of the sample. The sample was placed in the focal plane with a focal spot radius of $\omega_0 = 14.6 \pm 1.6\,\mu m$, (ellipticity ~ 0.89), which was measured using a charge-coupled device (CCD) sensor-based, beam diagnostic system (MicroSpot Monitor of Primes GmbH, Germany). Since the ellipticity of the focal spot is greater than 0.87 (ratio of minor to major axis of the spot), the beam profile is considered to have a circular power density distribution according to ISO 11146-1:2005(E) standard. We chose the maximum beam width, based on second order moment as described by the standard, as beam diameter for all the calculations in Sec. 3.3. The beam was directed perpendicular to the sample surface. The focus position was fixed for all the experiments and coincided with the original surface . No exhaust system was used to extract debris from the laser material interaction zone. The laser energy supplied to the surface was varied by using a combination of a half-wave plate and a linear polarizer. A pyroelectric detector (PM30 with FieldMax II of Coherent, USA) was used to measure the average laser power incident on the sample with an error less than 8%. The energy of the individual pulses was determined by dividing the measured average laser power by the pulse frequency. The power instability of the laser source is less than 2%. In this work, the laser pulse energy was kept at 135.6 μJ maximum and 3.3 μJ minimum. The laser-induced surface profiles are referred to as 'craters 'in the forthcoming sections. At a repetition rate of 8 kHz and a beam scanning velocity of 1 m/s, time between consecutive pulses on the same location equals 3.9 ms. The geometrical pulse-to-pulse distance was at least 125 μm and the number of pulses varied from $N = 1$ to 50 (1, 5, 7, 10, 15, 20, 25, 30, 50). A total of 21 craters were created per laser setting to get statistically sound values.

2.2. Material

Typical zinc (99.7%wt Zn, 0.3%wt Al) used for coating on steel products, was melted in a crucible at 460°C and cast by gradual cooling in a ceramic crucible. Then the sample was sectioned

followed by compression mounting in phenolic resin for metallographic analysis. Preparation procedures included grinding with SiC emery paper (18 μm and 10 μm grit size), polishing with 1 and 3 μm diamond suspension and final polishing with colloidal silica (0.04 μm) suspension. After polishing, an average roughness (R_a) lower than 30 nm was measured by confocal laser microscopy. The polished polycrystalline zinc sample had a minimum grain size of about 200 μm.

2.3. Analysis tools

Spectroscopic ellipsometry measurement (M-2000UI ellipsometer from Woollam, USA) was carried out on the untreated surface over a wavelength range from 245 to 1690 nm at 65°, 70°, 75° incident angles in order to obtain the optical constants, i.e. the refractive index n and extinction coefficient k, of the polished sample. Craters were measured by means of Confocal Laser Scanning Microscopy (CLSM), (VK-9700 of Keyence Corporation, Japan). The lateral and vertical resolution of CLSM measurements were 276 nm and 1 nm, respectively. The crater morphology was analyzed by means of a field emission Scanning Electron Microscope (SEM), (JSM-7200F of Jeol, Japan). The chemical composition of the samples was examined by X-ray Photoelectron Spectroscopy (XPS), (Quantera SXM of Physical Electronics, USA). XPS spectra were obtained using an aluminum anode (Al Kα= 1486.6 eV) operating at 12.5 W and a spot size of 50 μm. The background pressure was $< 2.5 \times 10^{-8}$ Torr. During measurements, the pressure was $\sim 2 \times 10^{-7}$ Torr mainly due to outgassing from the phenolic resin mount. A full XPS profile along a certain depth of the sample was determined at 50 W with 200 μm spot size, after sputtering the surface of the sample with Ar ions with a beam energy of 1 and 3 keV.

3. Results & discussions

The optical constants n and k of the zinc sample measured by ellipsometry are shown as the inset in Fig. 1. The reflection (R) coefficient for a perpendicular incident laser beam is calculated from these constants as [31]
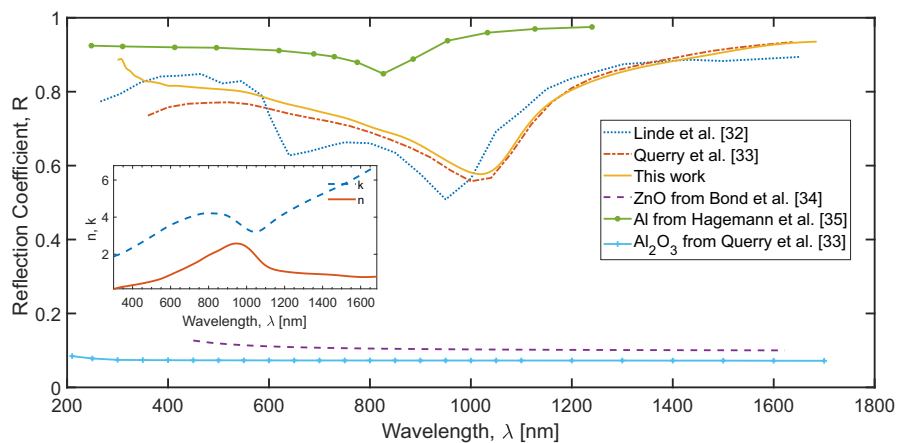
$$R = \frac{(1 - n)^2 + k^2}{(1 + n)^2 + k^2} .$$

(1)

Fig. 1. Reflection coefficient R, of zinc for corresponding wavelengths calculated from the n and k values from Ref. [32, 33] and from ellipsometry measurement on the sample under investigation using Eq. (1). The inset shows measured n and k values of this work.

Figure 1 shows this calculated R as a function of the wavelength. The values obtained from other sources for pure zinc [32, 33], zinc oxide (ZnO) [34], aluminum [35] and aluminum oxide

(Al_2O_3) [33] are also plotted in this figure for comparison. The choice of the laser processing wavelength of 1030 nm in this work follows from the lowest reflectivity around 1000 nm at room temperature, as well as increased absorption from the elevated electron temperature [24, 36]. It is worth noting that the reflectivity of ZnO and Al_2O_3 is low for all wavelengths. Therefore, any native oxide layer present would have negligible effect on the absorption of the laser beam.

3.1. Crater morphology

Figure 2 shows SEM images of ablated craters in Zn as a function of the number of pulses ranging from N=1 to 50 and as function of the peak laser fluence levels ranging from $F_0 = 0.98$ J/cm^2 to 40.8 J/cm^2. It is apparent from this figure that the morphology of the craters depends both on the peak laser fluence and the applied number of pulses. Although the craters are disc-shaped at low
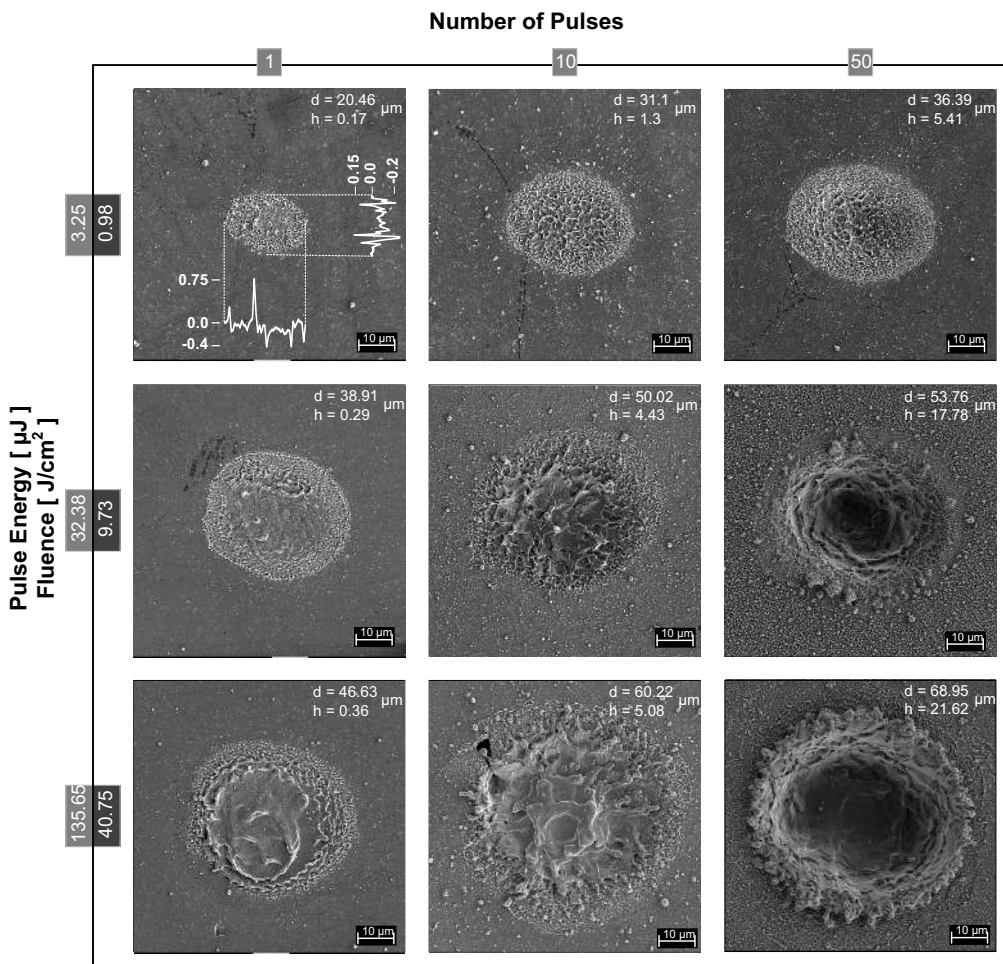

Fig. 2. SEM images (top view) of zinc surface irradiated at different laser pulse energies E_P and corresponding peak fluence F_0 levels (rows) and at different number of laser pulses N (columns). Diameter, d and maximum depth, h of the modified surface are derived from CLSM measurements. All images are in same scale. Corresponding crater profile, measured from CLSM measurements, is shown in the top-left image.

fluence, they become more splash-dominated with increasing F_0 and N. Within the range of

parameters studied, no 'melt-free' craters were observed. As can be observed from the inset texts, maximum depth (h) and diameter (d), measured by CLSM, increases with increasing number of pulses and laser fluence. However, the well-known upper limit in the increase of the diameter and depth was not observed within our experimental conditions [37]. Even at the lowest fluence and single pulse (N=1) processing, evident signs of melting are visible in terms of 'exploding bubbles', jets with spherical endings and thin membranes, which surround scratches on the sample surface, see e.g. Fig. 3. These submicron features are sparsely distributed at the center part of the crater and follow a cell-like structure at the edge of the crater including (sub)microcavity, microrim and submicron protrusions with spherical tips of diameter up to 0.8 μm. Inside scratches (Fig. 3(b)), which were present on the surface prior to processing, small ripple like structures orthogonal to the scratch side wall are present along with the bubble burst rims similar to the scratch free surface. Similar features were observed by Oboña et al. for Cu surface processed with the same ps-pulsed laser source [38, 39]. With increasing fluence for single pulse processing, the sparse distribution of microprotrusions at the spot center become increasingly visible with cell-like submicron structures at the spot edge. Nano and submicron particle redeposition in the crater increases as well, see e.g. Fig. 3(c). At $F_0 = 9.73$ J/cm^2, melt expulsion occurs at the center of the spot and microstructures agglomerate at the edge of the crater. For single pulse processing, the average depth of the ablated craters ranges from 250 to 650 nm and the diameter of the modified area increases from about 20 μm to about 47 μm with increasing laser fluence. Since the plasma plume forms on a nanosecond time scale and expands rapidly in air [40, 41], plasma shielding is unlikely to occur within the 7 ps laser pulse irradiation. Therefore, the depth of the ablated crater is affected by the formation of a post-pulse plasma that is strong enough to push the melt towards the outer edge of the crater. This also indicates that a thick molten layer may have formed as a result of the laser irradiation of the sample.

At the lowest fluence level of $F_0 = 0.98$ J/cm^2, with increasing number of pulses, an increase of both the depth and the diameter of the craters is observed. The mean size of the microprotrusions gets larger with increasing N but reduces in the spot center. The microrims also get thicker and reveal expulsion and redistribution of the melt towards the edge. At $N = 5$, nano-roughness around the crater starts to appear, see e.g. in Fig. 3(d) part of which is marked with a white rectangle. Redeposition of submicron and microparticles around the craters becomes more prominent with increasing pulse number as can be seen for $N = 7$ and 30 in Fig. 3(d) and (e). However, for $N \geq 10$, there appears a 'halo' around the crater as shown in Fig. 3(e). Redeposition occurs outside the halo. This halo has a diameter of ∼ 48 μm, which coincides with the Gaussian beam diameter at 1% of the peak intensity of the laser spot. If the laser fluence is increased further, the halo begins to disappear. That is because expelled melt from the center in form of splash and particle redeposition from the ablation plume starts to cover the halo. From this point onward, the diameter of the ablated crater does not follow the common logarithmic dependency on incident fluence [5]. Details of this are discussed in Sec. 3.3.3. Eventually by melt expulsion, stacked splash 'fingers' form a rim around the crater at high fluence levels and/or number of laser pulses. For $F_0 \geq 10$ J/cm^2, melt splash fingers do not develop radially, rather randomly, around the crater center.

Using CLSM, the 3D morphology of the craters were measured. A shape detection algorithm was used to extract dimensions (diameter, depth, volume and surface area) of the crater from CLSM data. Noisy results can be expected due to surface irregularities, especially at low fluence levels and low number of pulses. Figure 4 shows cross-sections of normalized crater profiles at $F_0 = 9.73$ J/cm^2 (left) and 40.75 J/cm^2 (right) at different number of pulses. These two fluence values are representative for two ablation regimes (see Section 3.3 for details). As can be observed from Fig. 4(a), the cross-sections of ablated craters are Gaussian-shaped for all N for fluence level up to $F_0 = 9.73$ J/cm^2 but start to deviate from this shape at higher fluence levels (Fig. 4(b)). At the maximum fluence value used in this work, the crater shape differs
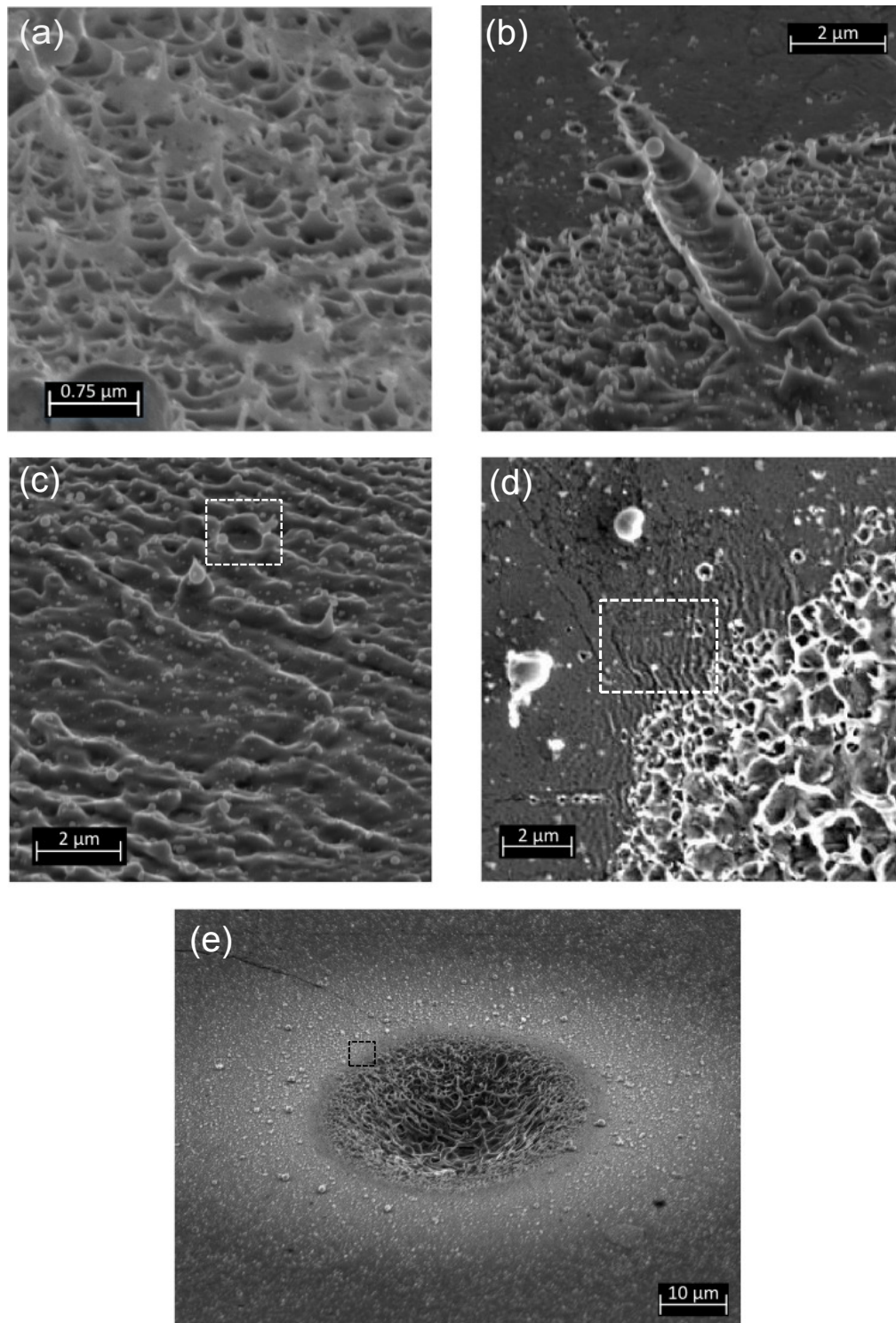
Fig. 3. SEM micrographs of characteristic surface structures on laser processed zinc surface. (a) jets with spherical endings at $N = 1$, $F_0 = 0.98$ J/cm^2 (tilted 70°), (b) thin membranes surrounding a scratch at $N = 1$, $F_0 = 6.87$ J/cm^2 (tilted 60°), (c) periodic surface structures at $N = 1$, $F_0 = 2.7$ J/cm^2 with a microrim marked with dashed rectangle (tilted 60°), (d) nano-roughness near the edge of the crater at $N = 7$, $F_0 = 0.98$ J/cm^2 marked with dashed rectangle (top view), (e) ablated crater at $N = 30$, $F_0 = 3.61$ J/cm^2 with 'halo' around the crater, part of which is marked with dashed rectangle (tilted 60°).
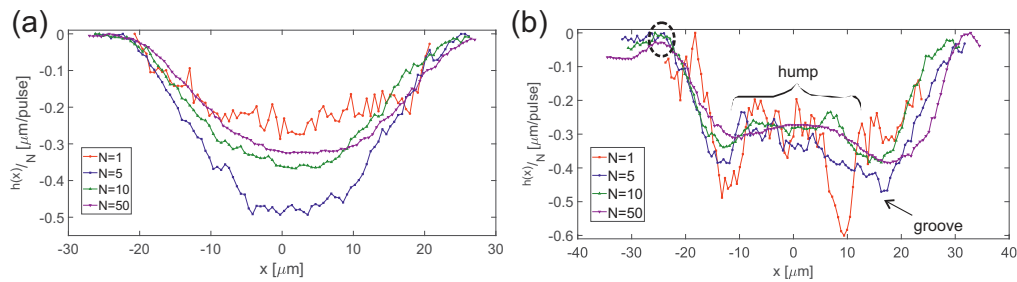
Fig. 4. Cross-sections (obtained from CLSM measurements) of ablated craters normalized by corresponding number of pulses N at (a) $F_0 = 9.73$ J/cm^2 and (b) $F_0 = 40.75$ J/cm^2. The dashed circle in graph (b) represents rim around the crater.

significantly from a Gaussian profile, showing a 'hump' in the center and surrounded by a groove (see Fig. 4(b)). For example, at $N = 50$, the hump extends over $1/e^2$ beam diameter equally from the center of the crater. The height difference is ~ 10 μm from the deepest point. Since zinc has a positive temperature coefficient of surface tension [42], this hump could result from the thermocapillary flow of the superheated liquid Zn. A similar bulging shape was also observed for Si [43]. However, the origin of this effect is not understood yet and is a topic of future study. In Fig. 4(b), the typical rim is marked with dashed black circle which appears for $N \geq 20$. With increasing number of pulses, the rim size increases. These observations could be attributed to increased melt expulsion and redistribution at higher pulse energies.

3.2. Chemical composition

To investigate possible effect of the laser treatment on Zn, X-ray photoelectron spectroscopy analysis was performed at the center of the craters, as well as on the untreated sample for reference. The time difference between the laser processing and XPS measurement on the sample was approximately 3 weeks and in the meantime the sample was stored in a desiccator. In all the XPS spectra, zinc, oxygen, aluminum and carbon were found to be present. The average carbon concentration for all N is approximately 50%, with C1s binding energy of 284.8 eV referring to adventitious carbon [44]. In Fig. 5, the element-wise concentration of Zn, Al and O as function of N, processed at and around $F_0 = 10$ J/cm^2, is presented by offsetting the C concentration. The Al concentration is found to be less than 5% at its peak concentration for $N = 1$ and drops to ≤ 1 at% for $N > 7$ (Fig. 5, middle). The high concentration of Al on the surface has been previously observed for galvanized coatings which can be attributed to the material properties of Al, e.g. low solubility in and higher oxidation potential than Zn [45]. The Zn concentration rises up to $N = 7$ and remains relatively steady at increased number of pulses (Fig. 5, top). The high O concentration present on the unprocessed surface initially declines with increasing N unto $N = 7$ and then remains stable. Craters processed at F_0 values of 6.87 and 9.73 J/cm^2 indicate nearly same O concentration. For $F_0 = 12.61$ J/cm^2, the observed lower O concentration (Fig. 5, bottom) may be due to dissociation of O from zinc oxide due to higher energy supplied. This is supported by the fact that the Zn content at corresponding locations are higher for $F_0 = 12.61$ J/cm^2 (Fig. 5, top). The binding energy of Zn2p$_{3/2}$, Zn LMM and Al2p electrons are 1022.0, 988.9 and 73.7 eV respectively, which indicates that the zinc and aluminum are in the oxide state (ZnO and $\gamma - Al_2O_3$) at the unprocessed surface [46].

To quantify the oxide layer thickness on the surface, a depth profile was determined in two different Ar$^+$ sputtering voltages. The left and right parts of Fig. 6(a) are obtained with 1 kV and 3 kV argon ion beam respectively over a surface area of 3×3 mm^2. The inset of Fig. 6(a) shows
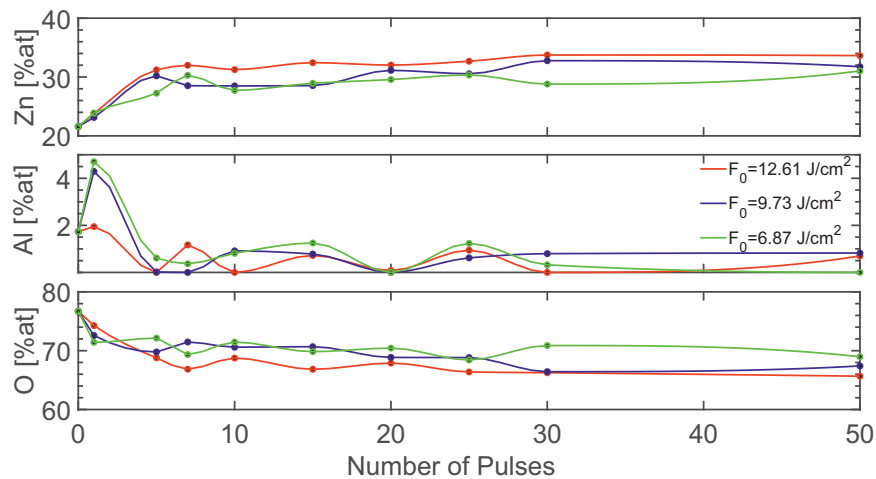
Fig. 5. Atomic concentration of Zn, Al and O for different number of pulses, N at F_0 =12.61, 9.73 and 6.87 J/cm^2.

the ratio of O to Al concentration. It can be seen that the high O/Al ratio present at the surface decreases sharply up to a depth of about 5 nm, after which, the O/Al ratio stays nearly constant up to ~ 47 nm depth. For comparison, the ideal O/Al ratio in Al$_2$O$_3$ is also shown in the figure as a dashed horizontal line. At around 50 nm depth, only Al and Zn are present as O concentration drops to near zero.

It should be noted that the purpose of Fig. 6 is to quantify the oxide layer thickness on the unprocessed virgin surface which is relevant for the first laser pulse. In contrast, the purpose of Fig. 5 is to quantify the effect of surface irradiation with different number of laser pulses on the chemical composition. Thus, Fig. 5 and Fig. 6 quantitatively refer to different depth levels. On SiO$_2$, the sputter rate is about 1.4 and 11.6 nm/ min for 1 and 3 keV ion energies respectively. The sputter rate for ZnO is approximately the same as for SiO$_2$ [47]. Therefore, sputter depths mentioned in Fig. 6 are approximated from the sputter rate of SiO$_2$. From the sputtering results it can be concluded that a thin carbon rich layer, ~ 1 nm, covers the sample. After removal of this carbon layer, a sharp transition is observed in the atomic concentrations of Zn, Al and O in Fig. 6(a). In Fig. 6(c), Zn2p$_{3/2}$ spectra are shown at different sputter depths, where the dashed and solid vertical lines at 1020.8 and 1022.5 eV denote the binding energies of Zn and ZnO respectively. The peaks of Zn2p$_{3/2}$ spectra are more inclined towards the ZnO line up to 4 nm and then shift towards the Zn line as the sputter depth increases. This indicates that there is only a thin zinc oxide layer of ~ 5 nm present. After about 5 nm, this zinc oxide has been removed and Zn appears. However, oxygen is still present as evidenced from Fig. 6(a). Figure 6(d) shows the Al2p spectra at various sputter depths, where the binding energies of Al and $\gamma - Al_2O_3$ are indicated by the dashed and solid vertical lines at 72.9 and 74.0 eV respectively. Unlike the Zn2p$_{3/2}$ peaks, the Al2p peaks shift from the Al line towards the Al$_2$O$_3$ line with increasing sputter depth. It suggests that an Al$_2$O$_3$ layer forms at a depth of about 5-6 nm (below the ZnO rich layer of about 5 nm) and extends to a depth of about 50 nm. Based on the above analyses, it may be concluded that the bulk Zn is covered by oxide rich layers of Zn and Al whose approximate thicknesses are indicated in Fig. 6(b).

3.3. Fluence ablation threshold

The fluence ablation threshold of materials, based on geometric features, has been determined in literature using different methods including:
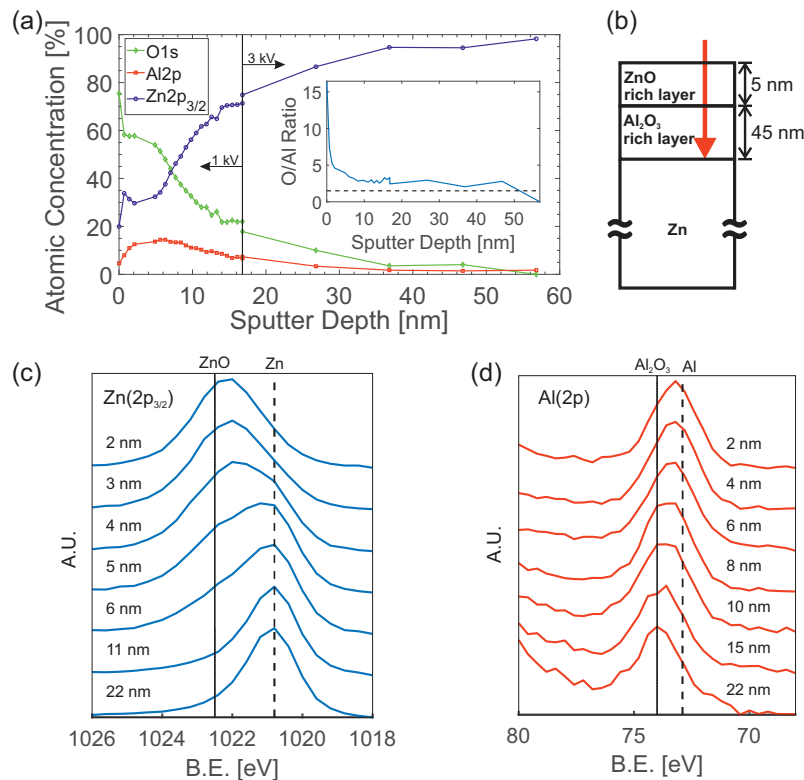
Fig. 6. Ar ion sputtering on unprocessed zinc surface. (a) Depth profile at low (left) and high (right) Ar ion energies shown by arrows. Inset shows the ratio of O and Al concentration as a function of sputter depth. Dashed horizontal line shows the O/Al ratio of Al_2O_3. (b) Schematic representation of native oxide layers on bulk zinc, red line indicates laser beam at 1030 nm. (c) Zinc ($Zn2p_{3/2}$) spectra and (d) Aluminum (Al2p) spectra at different sputter depths during 1 keV Ar^+ sputtering. The dashed and solid lines represent the binding energies of the corresponding metal and its oxide.

- extrapolating fitted measurement data of the semilogarithmic relationship between the ablated crater diameter squared and the laser fluence [5, 17],
- ablation rate per unit of fluence in terms of ablated depth [6, 16],
- ablation rate per unit of fluence in terms of ablated volume [7, 13, 19].

In this research, all three methods are used and compared for the first time, with a focus on the characterization of the ablation process of zinc, starting with the volume ablation rate method. It is worth noting that the accuracy of the calculation depends on the accuracy of the measurement. Accurate measurement of diameter is difficult because the exact boundary between the processed and unprocessed area is difficult to distinguish. In this work, features visible in optical microscopy were considered as a reference. The affected area has been determined from the optical microscopy image. Such an image was superimposed on the corresponding confocal microscopy image to determine the diameter, depth and volume data.

3.3.1. Ablated volume per pulse

The spatial fluence profile F [J/cm^2] of a laser beam with a Gaussian fluence distribution in polar coordinates (r, z, ϕ) is expressed as,

$$F(r, z, \phi) = F_0 \cdot \exp\left(-\frac{2 \cdot r^2}{\omega_0^2}\right) \cdot \exp\left(-\frac{z}{\delta_e}\right) , \qquad (2)$$

where, ω_0 denotes the beam spot radius $(1/e^2)$, δ_e is the effective energy penetration depth and F_0 is the peak fluence which is related to the pulse energy, E_p as $F_0 = (2 \cdot E_p)/(\pi \cdot \omega_0^2)$. The ablated volume per pulse ΔV can be expressed as [18, 48]

$$\Delta V = \frac{1}{4} \cdot \pi \cdot \omega_0^2 \cdot \delta_e^V \cdot \left[\ln\left(\frac{F_0}{F_{th}^V}\right)\right]^2 , \qquad (3)$$

where δ_e^V and F_{th}^V are fit parameters representing energy penetration depth and threshold fluence respectively. For laser-induced craters in this study, the ablated volume per pulse is plotted against
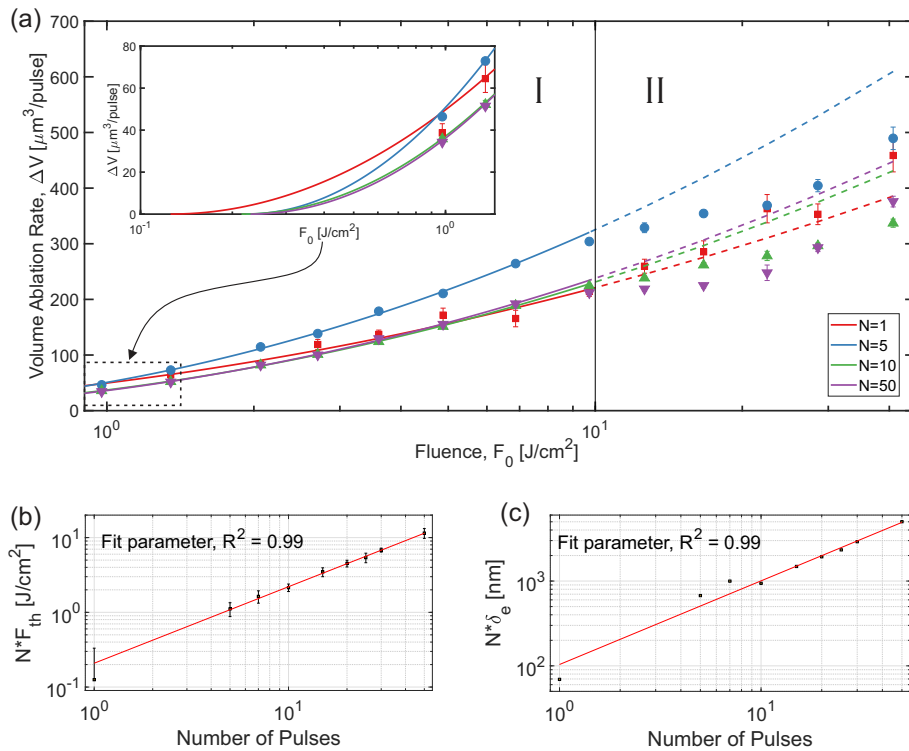

Fig. 7. (a) Ablated volume per pulse ΔV as a function of peak fluence F_0. The solid curves represent the least squared fit according to Eq. (3) in regime I only and dashed curves are extensions of the solid curves in regime II. Inset shows the extrapolated curves to $\Delta V = 0$. (b) Accumulated threshold fluence, $N \cdot F_{th}(N)$ as a function of laser pulse number N. The solid curve represents a least squared fit according to Eq. (4). (c) Accumulation in energy penetration depth as a function of laser pulse number, N for $\omega_0 = 14.6$ μm. The solid line represents least squared fit according to Eq. (5). Note that the error bars are smaller than the data points.

peak fluence F_0, in Fig. 7(a). The volumetric ablation rate ΔV was obtained from the 3D confocal

microscopic profile of the ablated crater and dividing by the number of laser pulses applied. In this figure, each data point represents a minimum of 5 craters to a maximum of 15 craters. The error bars are not visible in Fig. 7 as their sizes are smaller than the symbol sizes. As can be observed, the volume ablation rate increases quadratically up to about 10 J/cm^2 and follows a slower rate for larger fluence levels for all N. The solid curves in Fig. 7(a) represent nonlinear least squared fit of Eq. (3) with $\omega_0 = 14.6$ μm excluding the data points for $F_0 > 10$ J/cm^2. It appears that there are two different ablation regimes within the fluence regime studied. This suggests that, for $F_0 > 10$ J/cm^2 (regime II), the ablation mechanism shows a shift from a thermally-driven to a splash-dominated process, where the resulting surface structure is determined not only by the photo-mechanical and photo-thermal processes but also by the melt dynamics (see Fig. 2). In the following sections, we focus on only regime I ($F_0 < 10$ J/cm^2), because it is relevant for accurate processing of Zn whereas regime II is much more stochastic in nature.

With increasing number of pulses, the threshold fluence increases indicating an accumulative phenomenon in regime I. Several approaches have been reported in the literature to account for this accumulation phenomenon of the fluence threshold in materials by an incubation model [7, 15, 49, 50]. The most cited approach to relate the ablation threshold fluence $F_{th}(N)$ for N pulses to single pulse $F_{th}(1)$ is given by the non-physical power relation [15]

$$N \cdot F_{th}(N) = F_{th}(1) \cdot N^\zeta , \qquad (4)$$

where ζ is referred to as the incubation coefficient. This coefficient characterizes the nature of incubation within the material, as such $\zeta = 0$ (complete incubation), $0 < \zeta < 1$ (material 'softening'), $\zeta = 1$ (absence of incubation) and $\zeta > 1$ (material 'hardening') respectively [15]. Except for its shortcoming of not converging for $N = \infty$, the model predicts the incubation within the material satisfactorily for a relatively low number of pulses [50, 51]. Figure 7(b) shows the fitted data according to Eq. (4) as a solid curve. The least square fit through the data yields an incubation factor of $\zeta^V = 1.02 \pm 0.04$. Incubation in the material stems mainly from both heat and defect accumulation [15, 20]. Post analysis of the samples verified no influence of thermal effect from a given leading crater. That is, pulse-to-pulse separation was long enough to avoid heat accumulation from previous pulses. Single pulse ablation threshold, following from Eq. (4) and Fig. 7(b), equals to $F_{th}^V(1) = 0.21 \pm 0.03$ J/cm^2, which is 60% larger than the threshold value obtained for $N = 1$ from Fig. 7(a). However, the fit according to Eq. (3) also indicates that for increasing number of pulses, the effective penetration depth δ_e^V decreases, implying incubation behavior for the energy penetration depth [49]. In other words, the incubation in threshold fluence is always accompanied with incubation in penetration depth. Thus, a simple incubation formula can be derived for the case of δ_e similar to Eq. (4) as

$$\delta_e(N) = \delta_e(1) \cdot N^{\zeta_\delta - 1}, \qquad (5)$$

where $\delta_e(N)$ denotes the effective penetration depth due to N pulses, and where $\delta_e(1)$ is the effective penetration depth of a single pulse and ζ_δ is the corresponding incubation coefficient. In Fig. 7(c), the accumulated penetration depth, $N \cdot \delta_e(N)$ is plotted against the number of pulses, where the solid line represents the fit according to Eq. (5). The fit results in $\delta_e^V(1) = 104 \pm 40$ nm with $\zeta_\delta^V = 0.99 \pm 0.1$. The optical penetration depth δ_{opt} was calculated to equal 25 nm from measured n and k values (see inset of Fig. 1). The difference between δ_{opt} and $\delta_e^V(1)$ indicates that heat affected volume is dominated by the generation of ballistic electrons.

3.3.2. Ablated depth per pulse

A second method used to determine the single pulse ablation threshold fluence $F_{th}^L(1)$ is based on the ablation rate in terms of crater depth per pulse. The relation between ablation depth per

pulse L, peak fluence F_0 and threshold fluence F_{th}^L can be expressed with an effective energy penetration depth δ_e^L as [6]

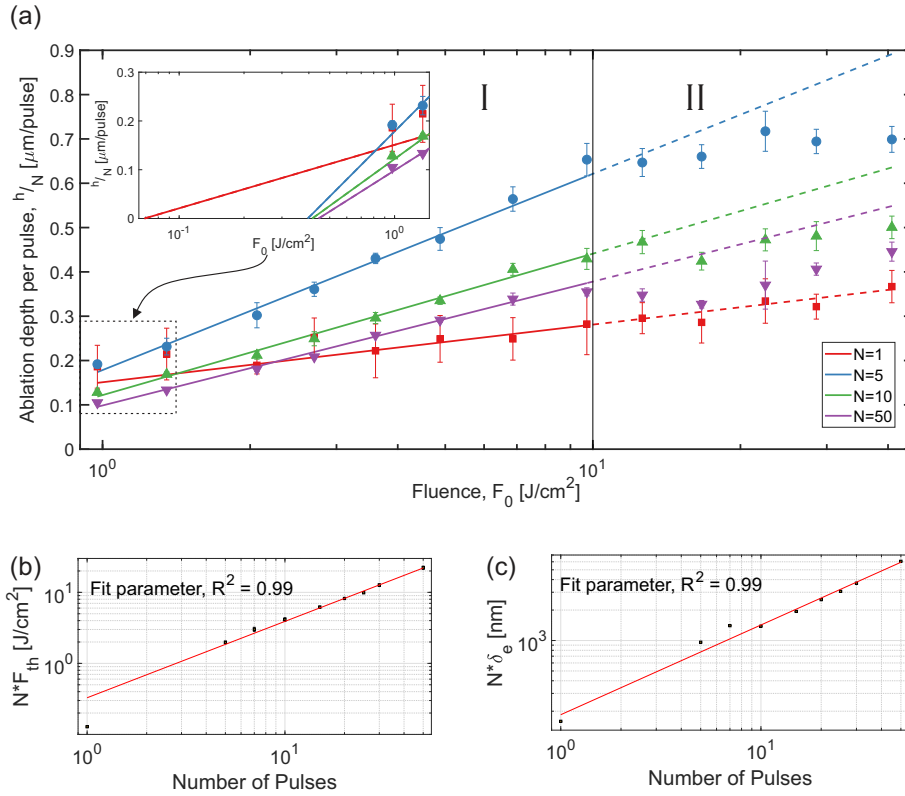$$L = \delta_e^L \cdot \ln\left(\frac{F_0}{F_{th}^L}\right) .$$

(6)

Fig. 8. (a) Ablation rates $L = \frac{h}{N}$ of Zn in air for different number of pulses N as a function of peak laser fluence F_0. The solid curves represent the least squared fit according to Eq. (6) in regime I and dashed curves are extensions of solid curves in regime II. Inset shows the extrapolated curves to $\frac{h}{N} = 0$. (b) Accumulated threshold fluence, $N \cdot F_{th}(N)$ as a function of laser pulse number N. The solid curve represents least squared fit according to Eq. (4). (c) Accumulation in effective penetration depth $N \cdot \delta_e^L$ as a function of laser pulse number, N. The solid line represents least squared fit according to Eq. (5).

There are two methods to determine the ablation rate L. In the first method, the ablation rate L can be determined by dividing the maximum crater depth h by the number of pulses N. Hence, the rate of ablation L can be calculated for different numbers of applied pulses as shown in Fig. 8(a). From the results of Fig. 5 and 6, it is clear that the ZnO and Al$_2$O$_3$ layer present on the sample surface is about 50 nm. On the other hand, Fig. 4(a) shows that a single pulse at $F_0 = 9.73$ J/cm^2 ablates about 250 nm. This means that the first pulse removes the oxide layer and the subsequent ablation is true representative for determining F_{th} and δ_e of Zn, since there is no interference from the oxide layers. This explains the observation seen in Fig. 8(a), where $N = 1$ shows the lowest ablation rate, which jumps to highest rate at $N = 5$ and then decreases for $N = 10$ and 50. Similar to the volume ablation rate ΔV, the crater depth increases with laser fluence until $F_0 = 10$ J/cm^2

and then decreases for increasing laser fluence. Therefore, data points for $F_0 > 10$ J/cm^2 (regime II) were excluded from curve fitting for all N. At $N = 1$, the scatter is too large for all F_0 values to fit. Looking at the fit trend for higher number of pulses, it is likely that the slope of the fit will be similar for $N = 1$. Moreover, presence of jets with spherical endings over the modified surface of the crater for $N = 1$, specially at low fluences (see e.g. Fig. 2(top-left image) and Fig. 3(a)), makes accurate depth measurement difficult. For these reasons, data points at $F_0 \leq 2.75$ J/cm^2 were excluded from the fitting procedure for $N = 1$. The incubation plot of the threshold fluences $F_{th}^L(N)$ is shown in Fig. 8(b). A linear fit according to Eq. (4) results in an incubation coefficient of $\zeta^L = 1.08 \pm 0.06$ with a single pulse threshold fluence of $F_{th}^L(1) = 0.33 \pm 0.06$ J/cm^2. As was concluded with respect to ablated volume incubation coefficient ζ^V, ζ^L also conforms that heat accumulation from previous pulses was avoided. Also, $F_{th}^L(1)$ is almost 1.6 times greater than $F_{th}^V(1)$. In Fig. 8(c), the accumulated penetration depth, $N \cdot \delta_e(N)$ is plotted against the number of pulses, where the solid curve represents the fit according to Eq. (5). The fit results in $\delta_e^L(1) = 182 \pm 66$ nm with $\zeta_\delta^L = 0.89 \pm 0.01$. This indicates a smaller degree of incubation than the value obtained using ablated volume, along with 56% overestimated $\delta_e(1)$.
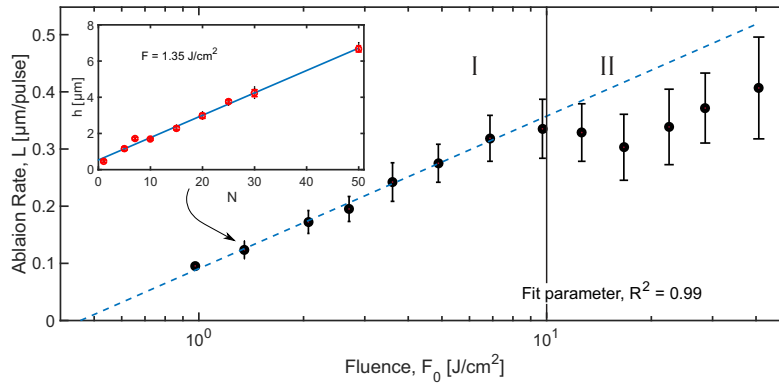

Fig. 9. Average ablation rate L of zinc in air for $N = 50$ as a function of peak laser fluence. The dashed line represents the least-squares fit according to Eq. (6). The inset shows the dependence of depth h on number of pulses N for $F_0 = 1.35$ J/cm^{-2}. The slope of the fit through the data points corresponds to average ablation rate, L [μm/pulse].

The ablation rate at a fluence level, or crater depth per pulse, can also be determined from the slope of the curve of the depth h as a function of number of pulses N. The inset in Fig. 9 shows the increase in crater depth h with the number of laser pulses N for $F_0 = 1.35$ J/cm^2. Assuming a linear dependence of the crater depth on the number of pulses, this gives $L = 0.12$ μm/pulse as an average rate of ablation depth per pulse. Figure 9 shows the ablation rate L obtained as a function of the peak fluence. In this figure, the dashed curve represents the nonlinear least squared fit of Eq. (6) which gives $\delta_e^L = 116 \pm 10$ nm and $F_{th}^L = 0.46 \pm 0.07$ J/cm^2. The effective penetration depth is in the same order of magnitude as $\delta_e^V(1)$ and $\delta_e^L(1)$, but differs by a factor of 1.1 and 0.6 respectively. The threshold fluence F_{th}^L determined using Eq. (6) represents the average ablation rate for $N = 50$ pulses. The determined value matches well with the threshold fluence for 50 pulses, $F_{th}^L(50) = 0.44 \pm 0.01$ J/cm^2 following Fig. 8.

3.3.3. Squared diameter vs. fluence

This method is referred to as the D^2 method, which is also the most widely used method as reported in literature [5, 14, 16, 17, 20, 50, 52]. The ablated crater diameter D is related to the peak fluence F_0 and the ablation threshold F_{th}^D as [5]

$$D^2 = 2 \cdot \omega_0^2 \cdot \ln\left(\frac{F_0}{F_{th}^D}\right) \, . \tag{7}$$

If the squared diameter D^2 measured from CLSM measurement data is plotted as a function of peak fluence F_0 in a semi-logarithmic scale, the fluence threshold F_{th}^D can be determined from a linear extrapolation to $D^2 = 0$. This graph can also be used to determine the beam diameter from the slope. However, the calculated beam diameter from the slope need not necessarily reflect the actual beam diameter, due to the change in absorption within the irradiated zone for multiple pulses [20, 50]. In the context of the current work, it is found that the crater diameter changes linearly with the increasing fluence as long as the halo as shown in Fig. 3(e), is unaffected by particle redeposition and melt expulsion. As soon as the halo (diameter ~ 48 μm) around the crater starts to 'disappear', the crater diameter increases randomly with increasing fluence. Figure 10(a) shows on a semilog scale the squared diameter D^2 of the ablated crater as function of the laser peak fluence for different numbers of pulses. As can be observed, the measured crater diameters deviate from the linear trend, within the laser parameters studied, as soon as they exceed a diameter value of ~ 48 μm (horizontal line in Fig. 10(a)). Moreover, the ablated diameter is insensitive to the change in the ablation regime (I or II) contrary to the observed behavior in the ablated volume and depth data discussed in Section 3.3.1 and 3.3.2 respectively. Therefore, instead of using the vertical line denoting the ablation regimes, data points lying above the horizontal line in Fig. 10(a) were omitted from the curve fit according to Eq. (7). At high fluence levels, 'tails' of the Gaussian intensity profile of the laser beam are intense enough to cause material modification. Thus, the crater diameter fails to follow the linear trend.
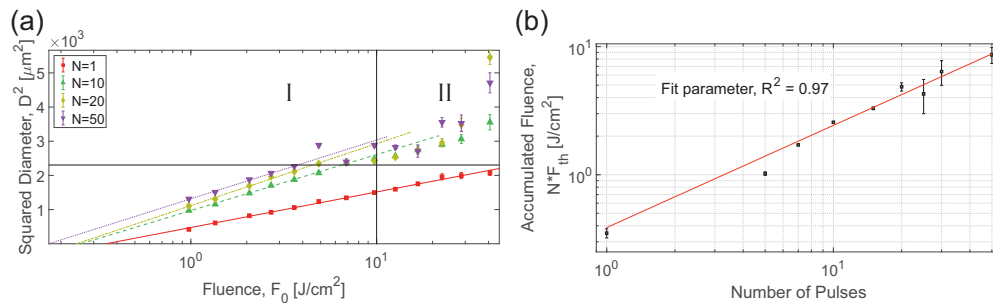

Fig. 10. (a) Squared diameter D^2 of the ablated crater for different number of pulses as a function of the peak laser fluence (log scale). The solid curves represent the least squared fit according to Eq. (7). The horizontal line at ~ 2500 μm^2 represents halo diameter. (b) Accumulated threshold fluence, $N \cdot F_{th}(N)$ as a function of laser pulse number N. The solid curve represents least squared fit according to Eq. (4).

The fitted curves in Fig. 10(a) possess similar slopes except for $N=1$. From the slopes of the curves for $N > 1$, the average value of the beam radius on the surface of the sample was derived to equal $\omega_0 = 18.6 \pm 1.1$ μm, which is about 22% larger than the optically measured beam diameter of $\omega_0 = 14.6 \pm 1.6$ μm (see Section 2). However the obtained ω_0 for $N=1$ is 15.0 ± 0.3 μm, which is only 2.7% higher than the measured value. Therefore, not only the D^2 method can

predict the actual beam diameter for $N=1$, but also it shows that the initial condition of the virgin surface changes such that the laser material interaction zone is effectively increased by about 22% after first laser pulse and stays constant within the range of parameters studied. Extrapolating the curves in Fig. 10(a) to $D^2 = 0$ results in the fluence threshold $F_{th}^D(N)$ for the respective number of pulses. From Fig. 10(a), an accumulation in threshold fluence seems apparent as threshold fluence decreases with increasing number of pulses. Figure 10(b) shows the curve fit of Eq. (4), where the last four data points have larger error bars than the rest of the data points. These large spreads in $F_{th}^D(N)$ originates from the fact that the number of qualifying data points for fitting Eq. (7) decreases for higher number of pulses as the diameter value exceeds the horizontal line in Fig. 10(a). The least square fit through the data yields an incubation factor of $\zeta^D = 0.8 \pm 0.2$ indicating a relatively strong accumulation effect when compared to the depth and volume analyses. The fit of Eq. (4) also results in a single pulse ablation threshold of $F_{th}^D(1) = 0.39 \pm 0.21$ J/cm^2. It may be noted that the spread in $F_{th}^D(1)$ is approximately 53% showing that diameter method, for ps pulsed laser processing of Zinc, yields the least reliable data when using Eq. (4) to derive single pulse threshold value in comparison to the volume and the depth methods. However, the calculated threshold value is very close to $F_{th}^L(1)$. Nevertheless, if the derivation of $F_{th}^D(1)$ is obtained directly from Fig. 10(a) (0.35 ± 0.02 J/cm^2) and not following Eq. (4), D^2 method is also reliable from the error estimate point of view.

3.3.4. Discussion

All the threshold fluence, energy penetration depth and incubation coefficient values obtained directly for single pulse ablation as well as from the fit of Eq. (4) for different methods are collated in Table 2. It should be noted that the incident laser fluence was calculated from the maximum beam diameter. The use of this maximum diameter of the elliptical spot, instead of the minimum diameter, results in an underestimation in the derived F_{th} and δ_e by 25.23% for all methods, but does not affect the corresponding incubation coefficients.

Table 2. **Results Obtained for Single Pulse Ablation Thresholds and the Incubation Coefficients for Polycrystalline Zinc.**

Calculation Method	Using the fit of Eq. (4) and (5)				From CLSM data of $N = 1$	
	$F_{th}(1)$ [J/cm^2]	ζ [-]	$\delta_e(1)$ [nm]	ζ_δ [-]	$F_{th}(1)$ [J/cm^2]	$\delta_e(1)$ [nm]
Volume	0.21 ± 0.03	1.02 ± 0.04	104 ± 40	0.99 ± 0.1	0.13 ± 0.13	69 ± 44
Depth	0.33 ± 0.06	1.08 ± 0.06	182 ± 66	0.89 ± 0.1	0.06 ± 0.003	54 ± 13
Diameter	0.39 ± 0.21	0.8 ± 0.2	n.a.	n.a.	0.35 ± 0.02	n.a.

It may be concluded from the results of this table that the single pulse threshold fluence values obtained in this work for $F_0 \leq 10$ J/cm^2 using three different methods (see Table 2) are of the same order of magnitude. For $F_0 > 10$ J/cm^2, the crater morphology becomes increasingly splash-dominated with increasing F_0 and N, resulting in a stochastic trend with larger spread in measured geometrical data. In Table 2, the error estimates in the first four columns originate from the fit of Eq. (4) and (5), whereas for the last two columns, they originate from the fit of Eq. (3), (6) and (7) for the respective calculation methods together with the spread in the CLSM data. In general, the threshold fluence and penetration depth values derived by fitting Eq. (4) and (5) and those obtained directly from the CLSM measurements differ noticeably. In relation to the rest of the data points for $N > 1$, the data point for $N = 1$ falls as an outlier in the fit of Eq. (4) and (5), as can be observed from Figs. 7(b)-7(c) and 8(b)-8(c). Moreover, the high error estimate corresponding to $F_{th}(1)$ using the volume method in column 5 represents the lack of determinism

in the ablation process for $N = 1$ as can be seen from the crater profile in Fig. 2 (top-left image). On the other hand, the low error estimate corresponding to $F_{th}(1)$ using the depth method in the same column is an underestimation of true error estimate, since the data analysis for $N=1$ in Fig. 8(a) does not incorporate the values for $F_0 \leq 2.75$ J/cm^2. For the fit results of Eq. (4) and (5), the volume method gives the lowest threshold fluence value, whereas the diameter renders the highest threshold value. The diameter method also shows higher degree of uncertainty. In contrast, both the volume and the depth method render relatively accurate values indicated by relatively lower error estimates in determining $F_{th}(1)$ and $\delta_e(1)$ as well as their respective incubation parameters. However, there lies a pronounced difference in the estimated $\delta_e(1)$ and ζ_δ obtained by these two methods. This could be attributed to the limitations of Eq. (6) that assumes constant reflectivity, post-pulse ablation and insignificant redeposition [6]. Also, the spread in measured data is larger for depth than for volume method.

Since both Al$_2$O$_3$ and ZnO are transparent for the laser wavelength of 1030 nm (see Fig. 1), as depicted schematically in Fig. 6(b), the laser energy absorbed in these oxide layers is negligible. However, for the absorbed part of the laser light within Zn, the Lambert-Beer law applies with an optical penetration depth δ_{opt}, within which the incident laser pulse with peak intensity I_0 decays exponentially [53]. The absorption of photons by the electrons creates a highly nonequilibrium state of so-called ballistic electrons, which penetrates deep into the material, causing electron-electron scattering, which thermalizes the electron subsystem [36]. The effective depth of the 'ballistic' electrons δ_{bal} can be roughly estimated as the product of Fermi velocity v_F and the Drude relaxation time τ_{drude} [54]. Therefore, as long as the sample thickness is greater than the penetration depth, the total (maximum) penetration depth of both photons and electrons becomes $\delta_{total} = \delta_{opt} + \delta_{bal}$. Using $v_F = 0.92 \times 10^8$ cm/sec [55] and $\tau_{drude} = 3.2 \times 10^{-14}$ sec [31] for zinc, the total maximum penetration depth δ_{total} in Zn is calculated to be about 55 nm. However, both δ_{opt} and δ_{bal} depend on electron temperature [52]. Since the melting points of ZnO (2248.15 K) and Al$_2$O$_3$ (2345.15 K) are significantly higher than Zn, presence of oxide layers ($h_{oxide} \geq \delta_{opt}$) may influence the temperature gradient between the electronic and lattice subsystems. The difference in the theoretical δ_{total} value and the calculated $\delta_e(1)$ value indicates that this native oxide layer thickness as well as the surface roughness ($R_a \sim 30$ nm) may also play a role for the effective energy penetration depth. The energy required for local vaporization within the energy penetration depth related to laser induced breakdown can be estimated to verify the calculated threshold fluences. Theoretically, the amount of fluence F_{th}^e required to evaporate material can be expressed as [56]:

$$F_{th}^e = \frac{\delta . \rho . \left((T_m - T_0) \cdot C_p + H_m + H_v\right)}{A} ,$$
(8)

where, $\rho, H_m, H_v, C_p, T_m, T_0, \delta$ and A represent the density of the solid (7140 kg $\cdot$ m^{-3} [21]), the enthalpy of fusion (111 $\times$ 10^3 J $\cdot$ kg^{-1} [8]), the enthalpy of evaporation (1748 $\times$ 10^3 J $\cdot$ kg^{-1} [8]), specific heat (0.382 $\times$ 10^3 J $\cdot$ kg^{-1} $\cdot$ K^{-1} [21]), melting point (692.68 K [21]), room temperature (300K), the energy penetration depth and absorption coefficient, respectively. Taking δ_{opt} of 25 nm and summation of $\delta_{total} + \delta_{oxide}$ of $\sim$ 100 nm for δ, Eq. (8) gives threshold values of 0.12 J/cm^2 and 0.47 J/cm^2 respectively. The calculated single pulse threshold fluences using all three methods lie within this range indicating a strong effect of ballistic electrons, as well as the surface chemical composition, in energy deposition within the material. For example, the fluence threshold and penetration depth values observed for $N = 1$ lying below the fitted line in Fig. 7 and Fig. 8 could follow from the presence of an oxide layer. Presence of a higher concentration of Al on the surface for $N \leq 7$ could explain the similar trend in ablation rate for $N > 7$ (see Fig. 4, Fig. 7(c), Fig. 8(c)). It indicates that for ps laser processing, the energy penetration depth is affected by material changes, such as surface oxidation, plastic deformation, crystalline growth etc., whereas optical changes, e.g. absorption variation, affect the threshold

fluence [49]. Although all three methods discussed in this work are derived from Eq. (2), there are practical advantages and disadvantages associated with these methods. For example, the diameter of a crater can be relatively easily determined from an standard/common optical microscopy, whereas a relatively expensive 3D profilometer is required for determining the depth and volume. Out of the three methods, the diameter method is the fastest, cheapest and computationally least expensive, whereas the volume method lies on the complete opposite end of the spectrum. However, the volume method considers the complete 3D effect of energy input and resulting crater geometry. Given that the crater morphology is irregular due to melt phenomenon, it is more logical to accept the values obtained using the volume method in this research work.

In relation with other reported threshold values, the threshold value reported in this work is in the same order of magnitude for $\tau_p \leq 1$ ps, and 6 times smaller than ns pulse duration. This suggests that, at a pulse duration equal or close to τ_{e-ph}, a mixture of non-equilibrium and equilibrium ablation mechanisms is responsible for material removal during laser ablation of polycrystalline zinc.

4. Conclusion

Within the boundary of our experimental conditions, picosecond pulsed laser ablation of zinc revealed two distinct ablation regimes. Although no significant chemical changes were observed with fluence variations, morphological observation shows that a shift from disc-shaped to splash-dominated crater geometry around 10 J/cm^2 marks the boundary between these two regimes. Three methods for determining the ablation threshold based on the volume, the depth and the diameter of the ablated crater respectively were compared with the associated incubation coefficients in order to find the best fitting method in the picosecond pulse duration. Because of the indeterministic nature in the ablation process originating from rapidly solidified molten features, the depth method was found to be prone to measurement uncertainty. Further, the diameter method results in better estimation of threshold fluence and beam diameter for single pulse processing than multiple pulses. However, this method was found to be less suitable for higher number of pulses and for determining subsequent incubation coefficient. Last, due to the higher dimensionality of the volume method, the lower error estimate in determining the threshold value and the melt morphology of the crater, the volume method was chosen to be the representative method for determining the ablation threshold and the energy penetration depth of Zn under picosecond pulsed laser irradiation. In the first regime (<10 J/cm^2), the ablation thresholds and the energy penetration depths for 1 to 50 pulses were measured and found to be independent of incident number of laser pulses as evidenced from an incubation coefficient almost equal to unity. In the second regime (>10 J/cm^2), this trend becomes stochastic in nature. Regardless of the processing parameter, molten features are always present. It was found that, a single 6.7 ps laser pulse at 1030 nm wavelength ablates bulk polycrystalline zinc in air under normal temperature and pressure when the incident beam fluence exceeds 0.21 J/cm^2. The energy penetration depth for a single pulse was found to equal 104 ± 40 nm. The strength of incubation in threshold fluence and energy penetration depth was found to equal $\zeta = 1.02 \pm 0.04$ and $\zeta_\delta = 0.99 \pm 0.1$ respectively, both of which were verified quantitatively with the ablated depth as a function of fluence. In the context of our work, picosecond laser processing of zinc in air results in a melt-dominated ablation process. For certain functionalities, such as applications involving tribology (roughness, friction), optics (visual appearance) or adhesion (paint, glue, lubricant), molten features might not necessarily be detrimental.